ISPRS Journal of Photogrammetry and Remote Sensing 162 (2020) 17–26

Contents lists available at ScienceDirect

ISPRS Journal of Photogrammetry and Remote Sensing

journal homepage: www.elsevier.com/locate/isprsjprs

Recent ENSO influence on East African drought during rainy seasons through the synergistic use of satellite and reanalysis data

Seonyoung Park[a,1], Daehyun Kang[b,1], Cheolhee Yoo[c], Jungho Im[c,*], Myong-In Lee[c]

[a] Satellite Application Division, Korea Aerospace Research Institute (KARI), Daejeon 34133, South Korea
[b] Department of Atmospheric Sciences, University of Washington, Seattle, WA 98195, USA
[c] School of Urban and Environmental Engineering, Ulsan National Institute of Science and Technology (UNIST), Ulsan 44919, South Korea

ARTICLE INFO

Keywords:
Drought indices
Teleconnection
Drought monitoring
Interannual relationship
Horn of Africa

ABSTRACT

This study identified a relationship between the El Niño-Southern Oscillation (ENSO) and East African drought during the two rainy seasons (i.e., short rain from October to December and long rain from March to May). ENSO shows a positive relationship with the East African short rain during the entire period analyzed (1949–2016). Meanwhile, a statistically significant relationship between ENSO and East African long rain appears only in a recent period (2000–2016), which is unprecedented in the past 50 years before the 2000s. The strengthened interannual relationship between ENSO and East African long rain is associated with distinguished Indian Ocean Walker cell in boreal spring, implying that their relationship could be affected by either multidecadal natural variability or anthropogenic forcing. Various satellite-based drought indices which consider vegetation health, land surface temperature, evapotranspiration, and precipitation with 1 km spatial resolution showed a robust relationship between ENSO and East African drought in the recent period (2000–2016) during the both rainy seasons. In the case studies of June 2005, August 2007, and November 2010, the anomalous wet condition in East Africa during the mature phase of El Nino became dry as La Nina developed in the following year, thereby a lagged response was observed in vegetation-related drought indices and long-term meteorological drought indices. Satellite-based high resolution (1 km) drought indices often showed heterogeneous drought patterns under the same drought condition from reanalysis data at coarse resolution (2.5°), indicating the importance of spatiotemporally continuous high-resolution measurements for drought monitoring in East Africa. Consequently, the synergetic use of high resolution satellite observations and reanalysis data is crucial to provide the effective monitoring, assessment, and seasonal outlook of East African drought.

1. Introduction

East Africa has experienced several severe droughts during the past 20 years due mainly to the decreasing rainfall trend in the rainy seasons (i.e., short rain from October to December and long rain from March to May, hereafter OND and MAM, respectively). In particular, the failure of the long rainy season in 2010/11 drove severe drought in East Africa (Lott et al., 2013; Lyon and Dewitt, 2012). The region from 30° to 52°E and from 10°S to 15°N in East Africa is called the Horn of Africa (HoA). Many studies have been conducted to examine what factors influence droughts in East Africa (Cattani et al., 2016; Anderson et al., 2012; Hastenrath et al., 2007). There are several research approaches and systems for early warning as well as drought monitoring in Africa. Severe drought has been monitored at some regional centers, such as the Agro-meteorological and Hydro-meteorological (AGHRYMET) Regional Center for West Africa, the Southern African Development Community (SADC) for southern Africa, and the IGAD Climate Prediction and Applications Center (ICPAC) for the HoA. ICPAC focuses on monitoring agriculture and water resources over the HoA and provides observation, satellite, and climate forecast data (e.g. rainfall, temperature, Standardized Precipitation Index (SPI), vegetation, crop monitor) over with decadal, monthly, and seasonal scale. The Famine Early Warning Systems Network (FEWS NET) from the USGS Center for Earth Resources Observation and Science (EROS) has developed various products using satellite data (i.e., NDVI) and rainfall forecasts for diverse spatiotemporal scales to monitor the drought in Africa. The FEWS NET water-balance model output and satellite-based products have been great sources for drought management in Africa (Senay & Verdin, 2003). Recently, the Land Surface Hydrology Group at Princeton University developed a system for seasonal hydrological forecasting and drought

* Corresponding author.
E-mail address: ersgis@unist.ac.kr (J. Im).
[1] The first two authors equally contributed to the paper.

https://doi.org/10.1016/j.isprsjprs.2020.02.003
Received 8 July 2019; Received in revised form 5 February 2020; Accepted 7 February 2020

monitoring in sub-Saharan Africa (Sheffield et al., 2014). The system is effective at estimating drought conditions by a combination of satellite-based remote sensing data (i.e., SMOS soil moisture index, NDVI, EVI), hydrological modeling, and seasonal climate forecasts.

Drought indices can diagnose drought conditions in various aspects over the wide areas of Africa using remotely sensed data with relatively high spatial resolution (~1 km). These drought indices have been formulated using various satellite-based surface variables including Land Surface Temperature (LST), Evapotranspiration (ET), Normalized Difference Vegetation Index (NDVI), and soil moisture (Bhuiyan et al., 2017; Lee et al., 2019; Padhee et al., 2017; Tadesse et al., 2017;Wang et al., 2016). Kogan (1990) suggested the vegetation condition index (VCI) that normalized NDVI at each pixel using the minimum and maximum values to eliminate the effect of geographic and environmental resources. Many blended drought indices can explain the complexity of drought. For example, the vegetation health index (VHI) proposed by Kogan (1995) improved VCI by adding Normalized land surface temperature (LST). The soil wetness deficit index (SWDI) was also proposed by combining NDVI and LST (Keshavarz et al., 2014). Rhee et al. (2010) suggested the scaled drought condition index (SDCI), combining NDVI, LST, and the Tropical Rainfall Measuring Mission (TRMM)-derived precipitation. The SDCI is well known to monitor agricultural and meteorological droughts in areas with various climate conditions. Zhang and Jia (2013) developed the microwave integrated drought index (MIDI) in order to monitor drought for a short time period, by combining LST, NDVI, and soil moisture. MIDI has been shown to detect metrological drought effectively compared to 1- and 3-month Standard Precipitation Indices (SPIs). Park et al. (2017) developed the High-resolution Soil Moisture Drought Index (HSMDI) by downscaling spatial resolution of Advanced Microwave Scanning Radiometer on the Earth Observing System (AMSR-E)-derived soil moisture from 25 km to 1 km. Both agricultural and meteorological droughts were well monitored by HSMDI. The drought indices using spectral-domain methods have also been developed. Ghulam et al. (2007b) suggested the Perpendicular drought index (PDI) using reflective and absorptive characteristics of canopy and soils in the NIR and Red wavelengths for monitoring drought in bare soil areas. Moreover, a modified perpendicular drought index (MPDI) has been developed to extend the use of PDI developed for bare soil to densely vegetated areas by considering the impact of vegetation coverage factors (Ghulam et al., 2007a).

The rainfall in East Africa is influenced by climate variability with both decadal (Tierney et al., 2013) and interannual time scales (Schreck and Semazzi, 2004). The El Niño-Southern Oscillation (ENSO), one of the prominent parameters indicating climate variability in the tropical Pacific Ocean, shows a possible impact on rainfall variability over Africa (Lyon, 2014). While most tropical land areas suffer drought during El Niño events (Lyon, 2004; Lyon and Barnston, 2005), drought in the HoA during the short rainy season (OND) is frequent in La Niña conditions (Lyon, 2014). The negative Indian Ocean Dipole (IOD) in developing La Niña years shows a dipole pattern of sea surface temperature (SST) with warming and cooling in the eastern and western Indian Ocean, respectively. These dipole SST patterns are associated with anomalous atmospheric overturning circulation which shows ascending (descending) motion in the Maritime Continent (HoA), which in turn lead to decreasing rainfall in the HoA. The ENSO-related IOD variations are prominent in boreal fall, while the IOD decays in boreal cold seasons (DJF and MAM) (Lu et al., 2018). Although the long rain (MAM) rainfall in the HoA is affected by La Nina-like SST patterns at a multidecadal time scale (Lyon and DeWitt, 2012; Lyon, 2014), the long rain tends not to be associated with large-scale SST including ENSO at an interannual time scale (Lyon, 2014). Hastenrath (2000) suggested that the long rain in the HoA is associated with a local descent of atmosphere rather than the overturning circulation over the Indo-Pacific region with a closed Indian Ocean Walker cell.

The objectives of this study are to (1) identify the interannual relationship between ENSO and drought in the HoA during the two rainy seasons (OND and MAM) during a recent period (2000–2016) and a long-term period (1949–2016) using ground and satellite observations, and climate reanalysis data and (2) diagnose drought due to the change of relationship between ENSO and East African rainfall using satellite-based drought indices. The relationship between ENSO and rainfall in the HoA (i.e. remote impact of ENSO) could be modulated by changes in the mean state and ENSO-property (Brands, 2017; Timmermann et al., 2018). From the aspect, we also analyze the long-term period (1949–2016) with 11- and 15-year moving windows to identify whether the result of the recent period (2000–2016) is sensitive to analysis period or not. In this study, three drought indices—Scaled Drought Condition Index (SDCI) (Zhang et al., 2017; Rhee et al., 2010), Evaporative Stress Index (ESI) (Otkin et al., 2013; Anderson et al., 2011) with high spatial resolution (1 km), and Standard Precipitation Index (SPI; McKee et al., 1993)—were used to analyze the effect of ENSO on East African drought in recent years (2000–2016). Satellite-derived data provide various surface factors (e.g., vegetation, LST, and ET) with high spatial resolution when compared to reanalysis data, while reanalysis data cover a longer temporal period (~40 years). Satellite-based high resolution drought indices are useful to monitor drought and assess the related damage especially at local scale. Therefore, the synergetic use of satellite observations and reanalysis data in this study can provide the effective monitoring and assessment of East African drought. The relationships between ENSO and rainfall in the HoA for the long-term period (1949–2016) were also examined using gauge-analysis precipitation and atmospheric reanalysis data because of the limited number of samples of satellite-based drought indices (17 years).

2. Study area

The study area is East Africa (30°E–52°E; 10°S–15°N). The area has a wide range of topography, ranging from low sea-level altitudes near the Indian coast to the Bale Mountains in Ethiopia, at over 4000 m (Fig. 4b). East Africa has two main rainy seasons. The precipitation in East Africa has a spatially heterogeneous pattern because the topography of the region at high altitudes, including the Ethiopian highlands, controls atmospheric circulation and meridional shift of the Intertropical Convergence Zone (ITCZ) leads to different precipitation patterns (e.g., bimodal or unimodal) (Hoell and Funk, 2014; Lyon, 2014; Nicholson and Kim, 1997). From January to July, the ITCZ shows northward shift from 15°S to 15°N, and convective activities in this low-pressure zone cause increasing amounts of cloud and precipitation, with convergence of low-level wind (Nicholson, 2018). The annual cycle of precipitation in the HoA is generally bimodal—short rains in OND and long rains in MAM (Fig. 1). In particular, during the two rainy seasons, convergence is strengthened in the ITCZ area, due to the influx of moisture from both the east and west.

3. Data and methodology

3.1. Satellite datasets

Drought indices were calculated using *in situ* observations and satellite data. SDCI was calculated using 8-day LST (MOD11A2), 16-day NDVI (MOD13A2) from the Moderate Resolution Imaging Spectroradiometer (MODIS) with the spatial resolution of 1 km and the Tropical Rainfall Measuring Mission (TRMM) 3B43 monthly rainfall with the spatial resolution of 0.25°. Three variables were converted into monthly data considering the number of days used in a month and then scaled 0 to 1 using a min–max scaling approach (0 represents dryness and 1 means wetness) (Rhee et al., 2010; Kogan, 1995). Rhee et al. (2010) developed SDCI by combining scaled LST (Temperature Condition Index; TCI), scaled NDVI (Vegetation Condition Index; VCI), and scaled TRMM (Precipitation Condition Index; PCI) (Eq. (1)). PCI from

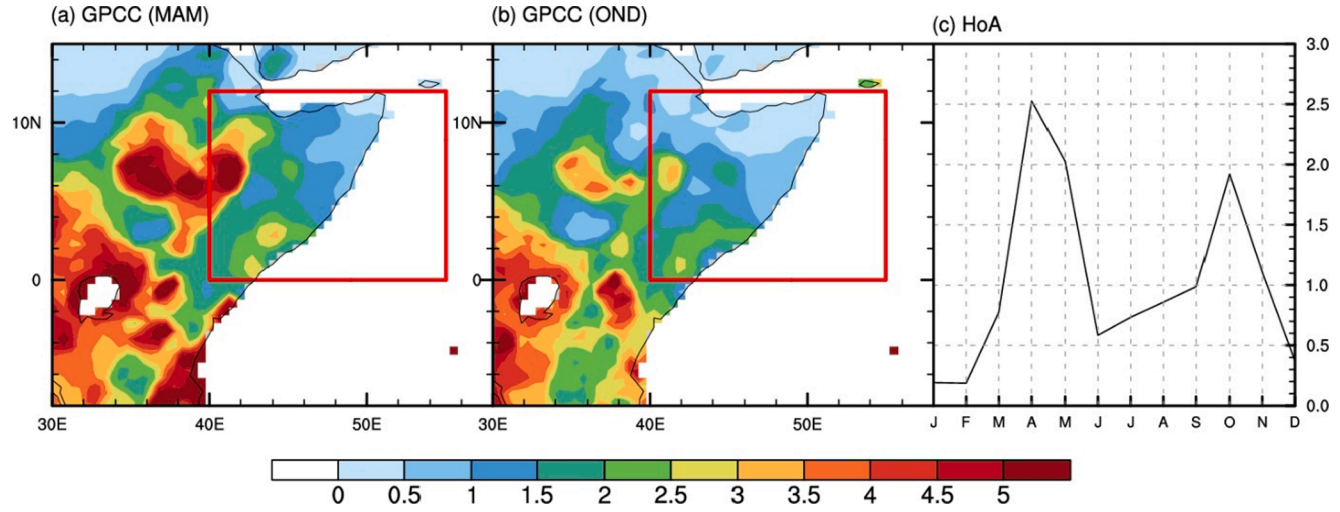

Fig. 1. Precipitation (mm/day) climatology for 1979–2016 during (a) MAM and (b) OND. (c) Area-averaged seasonal precipitation climatology in the HoA (land area in 0–12 N; 40-55E).

Table 1
The classification schemes of Scaled Drought Condition Index (SDCI) and Evaporative Stress Index (ESI) according to the U.S. Drought Monitor (USDM) category.

Drought category	USDM	SDCI	ESI
Exceptional drought	D4	0.0 to < 0.1	< −2.5
Extreme drought	D3	0.1 to < 0.2	− 2.5 to < -2.0
Severe drought	D2	0.2 to < 0.3	−2.0 to −1.5
Moderate drought	D1	0.3 to < 0.4	−1.5 to < −1.0
Abnormally dry	D0	0.4 to < 0.5	−1.0 to < −0.5
No drought	No Drought	0.5 to < =1	−0.5 to < =3

TRMM at different spatial resolutions (~27.75 km) was resampled using nearest neighbor to match the finest spatial resolution (1 km) to develop the blended drought index (SDCI). This index has been proven useful in monitoring drought in recent studies (Park et al., 2016; Du et al., 2013). The categories of SDCI were classified based on Rhee et al. (2010) matching with United State Drought Monitor (USDM) Drought Category (Table 1).

$$SDCI = 0.25 \cdot VCI + 0.25 \cdot TCI + 0.5 \cdot PCI \quad (1)$$

ESI was calculated using standardized anomalies of the fraction between monthly ET and potential ET (PET) at 500 m spatial resolution (MOD16A2) (Anderson et al., 2011). MODIS 8-day ET and PET were also merged monthly data as LST and NDVI. The categories of ESI matched with USDM and SDCI Drought Category are shown in Table 1. MODIS data (LST, NDVI, ET, and PET) were obtained from National Aeronautics and Space Administration (NASA) EARTHDATA (http://earthdata.nasa.gov), and TRMM data was obtained from Goddard Earth Sciences Data and Information Service Center (GES DISC).

3.2. Observation and reanalysis datasets

SPI was calculated using Global Precipitation Climatology Project (GPCP; Huffman et al., 1997) version 2.3 rainfall data between 1979 and 2016. The precipitation during the given period was transformed to a normal distribution by fitting it to probability distribution. Zero values of SPI represent the mean SPI for each station during the given period, with negative values meaning dryness and positive values meaning wetness (Edwards, 1997). The SPI can compute the precipitation deficit for multiple timescales which provide the information for short-term (early warning) and long-term (drought severity) drought. In this study, 1-, 3-, 6-, 9-, and 12-month cumulated precipitation deficits (SPI1, 3, 6, 9, and 12, respectively) were calculated.

The atmospheric reanalysis from the National Centers for Environmental Prediction (NCEP)/Department of Energy (DOE) was used for examining atmospheric circulation related to the ENSO. The Hadley Centre Sea-Ice and Sea Surface Temperature (HadISST; Rayner et al., 2003) version 1.1 (1° resolution) and the GPCP were used as gridded datasets of observational SST and precipitation, respectively. The Global Precipitation Climatology Centre (GPCC; Schneider et al., 2008) version 7 (1° resolution) precipitation data were also used to examine East African rainfall during the long-term period.

SST anomaly data in the NINO3.4 region (5S-5N; 120–170W) were used to represent ENSO during December-January-February (DJF). We compared the DJF-mean NINO3.4 index with East African drought

Table 2
Specification of the datasets used in this study.

Data	Product	Time period	Resolution	Source
MODIS	LST	2000-present	1 km	NASA EARTHDATA
	NDVI	2000-present	1 km	
	ET/PET	2001-present	500 m	
TRMM	Precipitation	1998–2018.09.30	0.25°	Goddard Earth Sciences Data and Information Service Center (GES DISC)
GPCP	Precipitation	1979-present	2.5°	Adler et al. (2003)
National Centers for Environmental Prediction-Department of Energy (NCEP-DOE) reanalysis 2	Atmospheric circulation	1979-present	2.5°	Kanamitsu et al. (2002)
HadISST	SST	1870-present	1°	Rayner et al. (2003)
GPCC	Land precipitation	1901-present	1°	Schneider et al. (2008)
Pacific Decadal Oscillation (PDO) index	PDO index	1854-present		National Centers for Environmental Information (NCEI)

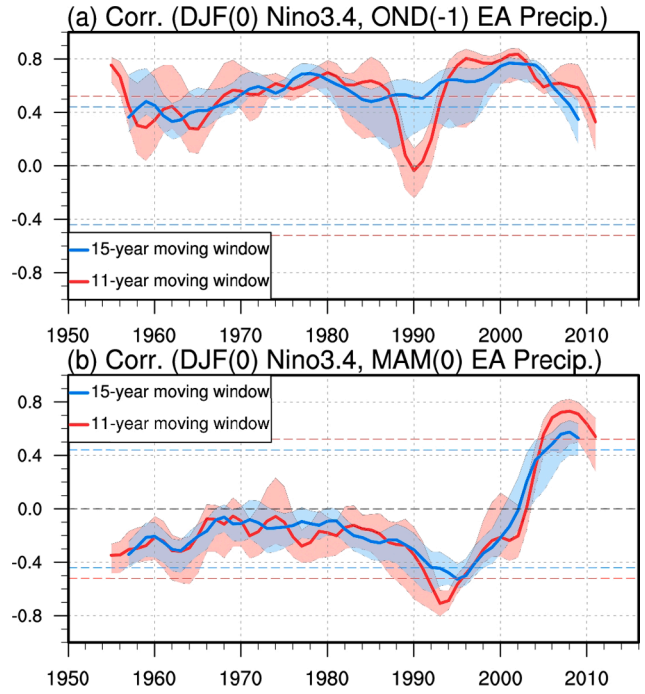

Fig. 2. (a) The correlation coefficient between the DJF-mean ENSO and the rainfall in the HoA (GPCC; land area in 0–12 N; 40-55E) during the preceding short rainy season with 11-year and 15-year moving windows for 1949–2016. (b) is the same as (a) but for the following long rainy season. Dashed blue and red lines refer to statistical significance at the 0.1 level for the 11-year and 15-year moving windows (degrees-of-freedom are 9 and 13), respectively. Shaded lines indicate minimum and maximum range of correlation coefficients using leave-one-out cross-validation of each moving window. The linear trend in each moving window was removed.

during the preceding short rain (OND) and the following long rain (MAM) to maximize the interannual variability related to the mature phase of ENSO. The specification of the datasets used in this study is summarized in Table 2.

4. Results and discussion

4.1. Decadal changes in the relationship between ENSO and East African precipitation

The interannual relationships between the mature phase of ENSO (DJF) and its preceding short rain (OND) and the following long rain (MAM) at an interannual time scale were examined. They show a statistically significant correlation during the short rainy season ($r = 0.5$, 99%), which is consistent during the entire period from 1949 to 2016 (Fig. 2a). The result averaged using an 11-year moving window shows a rapid decrease around the year 1990, which is caused by two abnormal conditions in 1989 and 1991. The HoA was too wet with neutral ENSO in OND 1989 and the HoA rainfall was moderate with strong El Niño in OND 1991, which may be associated with the volcanic eruption of Mt. Pinatubo. Nonetheless, the 15-year moving window shows a consistent positive correlation. While the long rain in the HoA and ENSO show a very weak correlation during the entire period ($r = -0.06$, 40%), both the 11-year and 15-year moving windows have shown a remarkable increase in correlation since the 2000s (Fig. 2b). The mature phase of ENSO shows high correlation with the Indian Ocean Basin Mode (IOB) (Zheng et al., 2011) during MAM ($r > 0.8$) (supplementary Fig. 1), indicating that the enhanced relationship between ENSO and the long rain in the HoA seems to occur through the IOB rather than the IOD (Saji et al., 1999). Due to the prominent autocorrelation of ENSO, the lagged relationships between DJF ENSO and long/short rains in the HoA are consistent whether we use a simultaneous ENSO index or not (not shown). The decadal change of the ENSO teleconnection to the long rain in the HoA might be associated with natural climate variability or anthropogenic forcing.

For example, the Indo-Pacific SST has shown a robust warming trend with a strengthening Pacific Walker circulation since the 1990s (England et al., 2014); this is associated with an increase in the zonal SST gradient in the equatorial Pacific Ocean. The strengthened zonal SST gradient thus plays a crucial role in the extension of the Pacific warm pool to the Indian Ocean, which could affect rainfall in the HoA (Williams and Funk, 2011). The dynamics of the relationship between the long-term SST change and the rainfall in the HoA have been discussed with a westward extension of the Pacific Walker circulation (Hoell and Funk, 2014). They suggested that the extended Walker circulation has had a strong influence on the HoA due to Western Pacific warming and the strengthening of the Walker circulation. The recent 20-year trend of SST and the drying HoA (Lyon and DeWitt, 2012) have been explained well by this mechanism. The recent change in the Indo-Pacific could be a possible modulator for the recent strengthening interannual relationship between ENSO and the long rain in the HoA.

The result in Fig. 3b suggests that the westward shift of the Walker circulation could be related to the interannual variability of ENSO teleconnection as well as the long-term trend. Anomalous ascending (around the dateline) and descending motion (around 120°E) in the tropics by the year-to-year variation of ENSO showed a westward transition from 2000 to 2016 (Fig. 3a and c). This westward transition also showed an extension of the ascending motion toward the HoA (40°–60°E), which is associated with the enhanced following long rain after El Niño events. The spatial distribution of the lagged ENSO teleconnection in MAM showed a northwest extension of the wet anomaly in the South Indian Ocean and well distinguished Indian Walker circulation, which is indicated as the upper level velocity potential with divergence (convergence) in the western (eastern) Indian Ocean for 2000–2016 (Fig. 3b and d).

4.2. Relationship between ENSO and satellite-derived drought indices in the recent decades

Fig. 4 shows the relationship between ENSO and the three drought indices in the HoA with MODIS land cover and Shuttle Radar Topography Mission (SRTM) Digital Elevation Model (DEM). We identified the spatial distribution of the correlations and averaged correlations between the DJF-mean ENSO index and three drought indices during the two rainy seasons over 17 years (Supplementary Fig. 2) of the HoA domain. Most of the drought indices showed strong correlations with ENSO during the two rainy seasons, and the correlations were almost the same when the linear trend of each variable was removed (Supplementary Fig. 3). While it has been considered that the drought in the HoA has had a possible interannual relationship with ENSO only during the short rainy season (Lyon, 2014; Nicholson, 2015), our results show that the relationship is also strong during the long rainy season. The correlation was strong for 6-month SPI during the long rainy season (Fig. 4k) and 1-month SPI during the short rainy season (Fig. 4h). The correlation between ENSO and the 6-month SPI during MAM is higher than that during OND because the preceding 6 months of MAM include the previous rainy season where there is a strong ENSO association, and the preceding 6 months of OND include rainfall during July and August, when the ENSO teleconnection is associated with dryness in northwest Ethiopia.

Fig. 5 shows the composition of two drought indices for El Niño and La Niña events. The HoA is wetter during El Niño events than La Niña ones in both rainy seasons because of the lagged interaction of the two seasons with tropical Indian Ocean SST (Supplementary Fig. 1) (Goddard and Graham, 1999). Table 3 shows the drought area (km^2) during the El Niño and La Niña events for the long rain seasons between 2000 and 2016. The drought area was calculated using FEWS rainfall

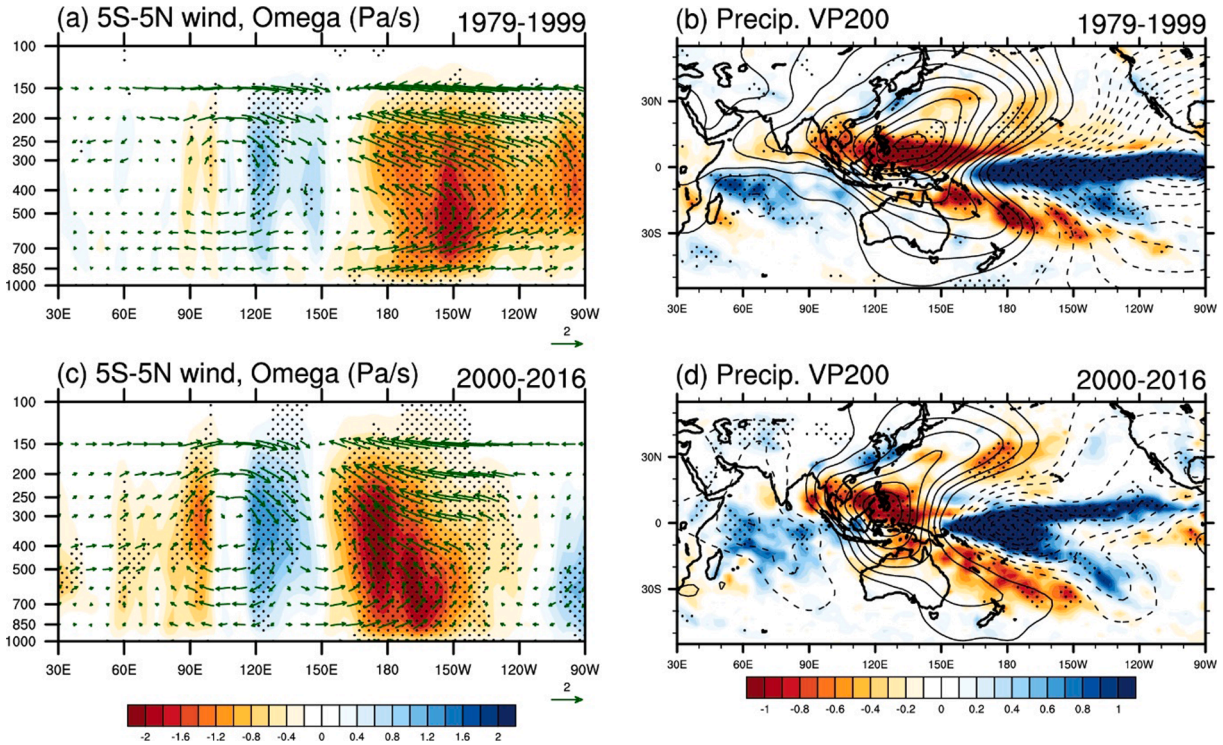

Fig. 3. (a) Regression of MAM vertical atmospheric velocity (shaded, 0.01 Pa s-1) and overturning wind vector (scale of vertical velocity is modified by multiplying 300) in the tropics (5°S-5°N) onto the DJF ENSO using the NCEP-DOE reanalysis for 1979–1999. (b) Regression of MAM precipitation (shaded, mm day-1), velocity potential at 200 hPa (contour interval is $2*10^5$ m^2 s^{-1}, dashed lines refer to negative) onto the DJF-mean ENSO index for 1979–1999. Bottom panels are same as top panels, but for 2000–2016. Dots indicate the statistical significance in the anomalous vertical velocity and precipitation at 5% significance level.

anomaly data. We identified drought where the anomaly is less than −10 mm. East Africa is considered a meteorologically complex region, and the temporal and spatial patterns of precipitation in East Africa vary with latitudes (due to the meridional shift of ITCZ) and topography (Levin et al., 2009; Nicholson, 1996). The Ethiopian and Kenyan highlands have dominant topography in East Africa (Fig. 4b), which channels and blocks the moisture transport at the lower level of the atmosphere (Levin et al., 2009; Viste and Sorteberg, 2013). The Ethiopian and Kenyan highlands are responsible for the existence of the Somalia jet along their topography. Consequently, northwestern Ethiopia showed an opposite pattern of drought compared to other Eastern Africa countries (e.g., Somalia, Kenya, Tanzania) during both rainy seasons (Figs. 4 and 5) due to the different timing of rainfall (Jun-August and unimodal), the Ethiopian highlands, and ENSO–West African Monsoon (WAM) teleconnection (Liebmann et al., 2014; Burrough and Thomas, 2013; Joly and Voldoire, 2009).

Since ENSO showed a statistically significant teleconnection to the rainfall in the HoA, the transitions of drought condition with the ENSO index were investigated. Fig. 6 shows the variations of various drought indices in three cases of decaying El Niño changing into La Niña (October 2004-May 2006, October 2006-May 2008, and October 2009-May 2011). A time lag effect between agricultural drought and ENSO was clearly detected in the results. One-month SPI, which is considered a meteorological drought index, depicts a direct response to the ENSO index while agricultural drought indices including SDCI, ESI, and 3- to 9-month SPIs, which are very useful in monitoring agricultural drought, show a time lag effect. ESI and SDCI have a similar pattern to drought conditions with 1- and 3-month SPIs as discussed in Otkin et al. (2016) and Park et al. (2017). The three cases in Fig. 6 show definite patterns from wet to dry conditions as ENSO changes from El Niño to La Niña. For example, the severe drought in 2011 due to the lack of long rain can also be explained from Fig. 6. As the ENSO index was converted from El Niño to La Niña between 2010 and 2011, the HoA suffered severe drought. OND in 2010 shows severe drought conditions (Fig. 6), and Lyon (2014) stated that OND in 2010 happened during one of the 10 driest years from 1950 to 2010.

4.3. Drought monitoring at different spatial scales

This study used high resolution satellite data to identify the relationship between drought and ENSO in the HoA during the recent period (2000–2016). Although satellite data are only available for the most recent two decades, it is crucial to use high resolution data to effectively monitor drought from local to regional scales. While 3-month SPI at 2.5° spatial resolution shows a wet condition in El Niño and a dry condition in La Niña, the spatial distributions of satellite-based drought indices show much more detailed and heterogeneous patterns (Fig. 7). Some regions suffered drought during El Niño, others had wet or normal conditions during La Niña (Fig. 7). It is considered that drought is affected by regional characteristics such as land cover (savanna and grassland in Fig. 4a) and water supply. Fig. 4. In addition, the difference of the spatial distributions in the correlations at different spatial scales was also shown in Fig. 4. High resolution drought indices relatively well reflected drought conditions caused by the topographical characteristics (e.g., highlands) in detail when compared to the reanalysis data.

Fig. 8 shows the temporal patterns of three drought indices (SPI, ESI, and SDCI) at a region in the HoA (i.e., the red box in Fig. 7). Although the tendency of droughts looks similar in all regions of HoA as in Figs. 4 and 6, the temporal patterns of drought indices are different at local scale. There are quite a few differences in the temporal patterns among the drought indices (Fig. 8). SPI showed the opposite drought patterns compared to SDCI and ESI (2002, 2003, 2008, 2014, and 2015 during MAM and 2002 and 2003 during OND) (Fig. 8). As discussed above, the scale issue is one of the reasons that resulted in the difference. Peng et al. (2019) compared the high resolution SPIE based on satellite precipitation data (CHIRPS with 5 km resolution) to coarse resolution SPIE, and concluded that high resolution data performed

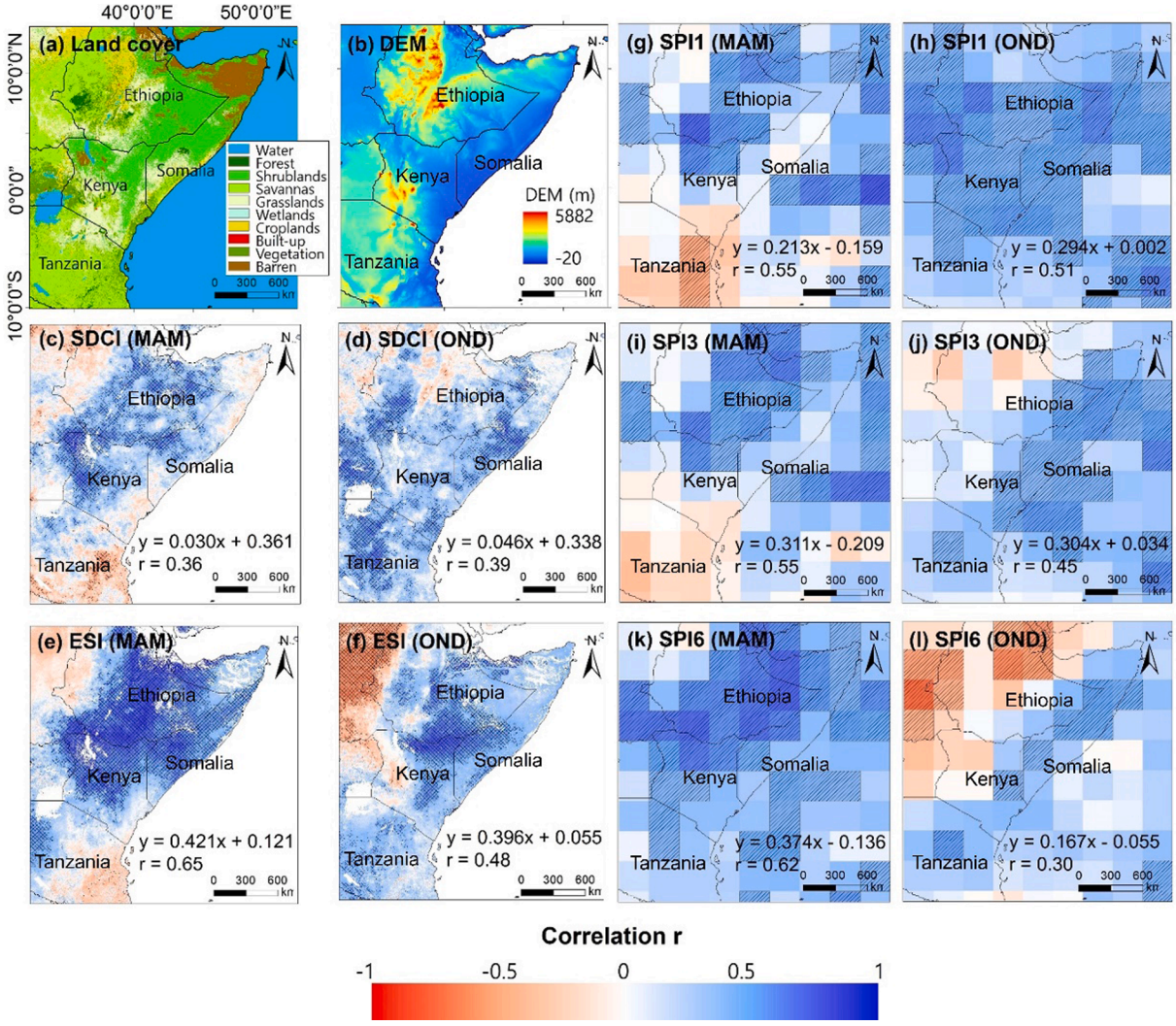

Fig. 4. (a) MODIS Land cover 2010 and sixteen land cover classes were aggregated to ten representative classes (e.g., Forest, Shrublands, and Savannas). (b) SRTM DEM over East Africa. (c-l) Spatial distribution of the correlations between drought indices, (c-d) SDCI, (e-f) ESI, and (g-l) SPI, and DJF-mean ENSO index for rainy seasons from 2000 to 2016. Areas with slashes indicate the statistical significance of correlation at the 10% significance level.

better for monitoring African drought. It is because high resolution SPEI can provide detailed information to identify societal impacts at local scale (e.g., sub-basin and district scales) in Africa (Peng et al., 2019). In addition, SPI was calculated only using rainfall data, while the other indices were developed considering various remote sensing-derived drought factors including surface temperature and precipitation with high spatial resolution.

The drought conditions of SDCI and ESI were also slightly different, although they showed broadly similar spatiotemporal patterns. In particular, the differences between two drought indices in 2010 (MAM), 2014 and 2015 (OND) were apparent (Fig. 8). As discussed in many studies including Lott et al. (2013) and Lyon and Dewitt (2012), East Africa suffered from severe drought in 2010/11 due to the shortage of rainfall during the long rain season. It is considered that SDCI that considers both precipitation and vegetation better detected the drought case than ESI. As drought cannot be explained only using precipitation because of the effect of artificial controls such as irrigation (Ryu et al., 2019), we expect that different types of indices can be useful to appropriately monitor and assess drought caused by different factors. Ryu et al. (2019) discussed the effect of agricultural drought caused by artificial controls through the comparison of various satellite-based drought indices, and suggested the use of an adequate drought index considering the corresponding drought characteristics. Since there is no absolute truth in drought, it is important to diagnose drought considering adequate drought factors to accurately monitor and assess various drought conditions. Thus, it is necessary to monitor and assess drought through the synergetic use of high resolution remote sensing observations and reanalysis data. It is possible to reinforce the merit and make up for the drawback because each has advantages from a different perspective.

Satellite-based high resolution drought indices may be applied to any area even with limited availability of *in situ* data such as East Africa (Bayissa et al., 2019). In addition, damage of drought under the same metrological drought (SPI) condition is different based the properties of drought indices. As mentioned above, more precise drought conditions can be identified from a multitude of perspectives using satellite-derived drought indices because satellite data can provide various surface factors such as LST, ET, vegetation health, soil moisture, and even inland water bodies (Asbury and Aly 2019; Barbosa et al., 2019; d'Andrimont and Defourny 2018; Park et al., 2016; Tran et al., 2017). Therefore, it is expected that the results of this study can be useful for the practical use in local or regional management of drought mitigation.

5. Summary and conclusion

East Africa, which is already vulnerable to drought, has experienced

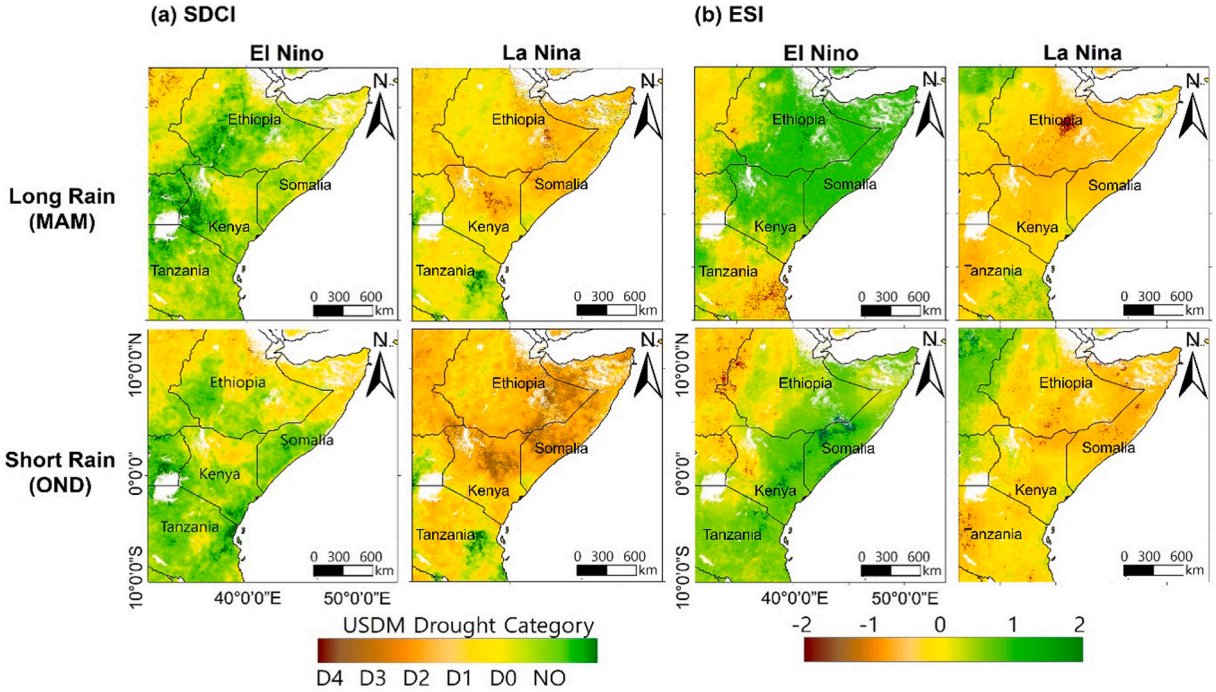

Fig. 5. Composition of drought indices, (a) SDCI and (b) ESI, for El Niño years (2003, 2005, 2007, 2010, 2015, and 2016 for long rains and 2002, 2004, 2006, 2009, 2014, and 2015 for short rains) and La Niña years (2000, 2001, 2006, 2008, 2009, 2011, and 2012 for long rains and 2000, 2005, 2007, 2008, 2010, 2011, 2016 for short rains) during the two rainy seasons. The categories of SDCI were classified based on Rhee et al. (2010) matching with USDM Drought Category (D4:0.0 to < 0.1, D3: 0.1 to < 0.2, D2: 0.2 to < 0.3, D1:0.3 to < 0.4, D0: 0.4 to < 0.5, No Drought: 0.5 to < = 1).

Table 3
Averaged drought area during the El Nino and La Nina events using FEWS rainfall anomaly data (long rains).

	Year	Drought area (km^2)
El Niño	2003, 2005, 2007, 2010, 2015, 2016	1,327,538
La Niña	2000, 2001, 2006, 2008, 2009, 2011, 2012	1,988,757

several severe drought events over the past 20 years. This study has identified the interannual relationship between drought in the HoA and ENSO in a recent period (2000–2016) and long-term period (1949–2016) using *in situ* and satellite observations, and atmospheric reanalysis data. The positive relationship between rainfall in the HoA and ENSO is stationary during OND and varies during MAM on a decadal time scale. While previous studies have discussed an unclear relationship between ENSO and East African drought during MAM (Hoell and Funk, 2014; Lyon, 2014; Maidment et al., 2015), ENSO and drought indices showed a statistically significant relationship during MAM as well as OND for 2000–2016, which is unprecedented in the past 50 years before the 2000s. Not only the station-based drought index considering precipitation but also satellite-based drought indices considering surface factors such as LST, vegetation, and evapotranspiration showed a robust relationship between drought and ENSO. For example, the drought conditions changed from wet to dry with the ENSO transition from the three cases when El Niño turned into La Niña. A lag time effect was also observed in vegetation-related drought indices and long-term meteorological drought indices. Satellite-based drought indices with high resolution provided more specific drought information than the station-based drought index using reanalysis data with coarse resolution. Satellite-based drought indices showed heterogeneous drought patterns under the same metrological drought condition-derived ENSO. Such heterogeneous patterns heavily depend on land cover. Thus, as discussed in Bayissa et al. (2019), satellite-based drought indices are useful to monitor drought especially in East Africa because of the availability of spatiotemporally continuous and reliable

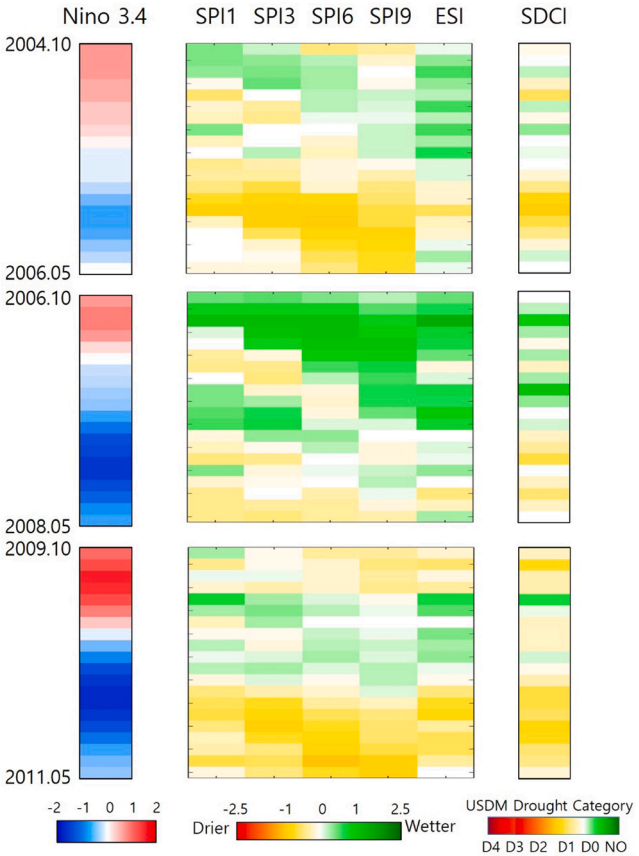

Fig. 6. Temporal evolution of drought (monthly) in the HoA as the ENSO index declined from El Niño to La Niña (October to May) in 2004–2006, 2006–2008, and 2009–2011. The categories of USDM are the same as the categories of SDCI in Fig. 5.

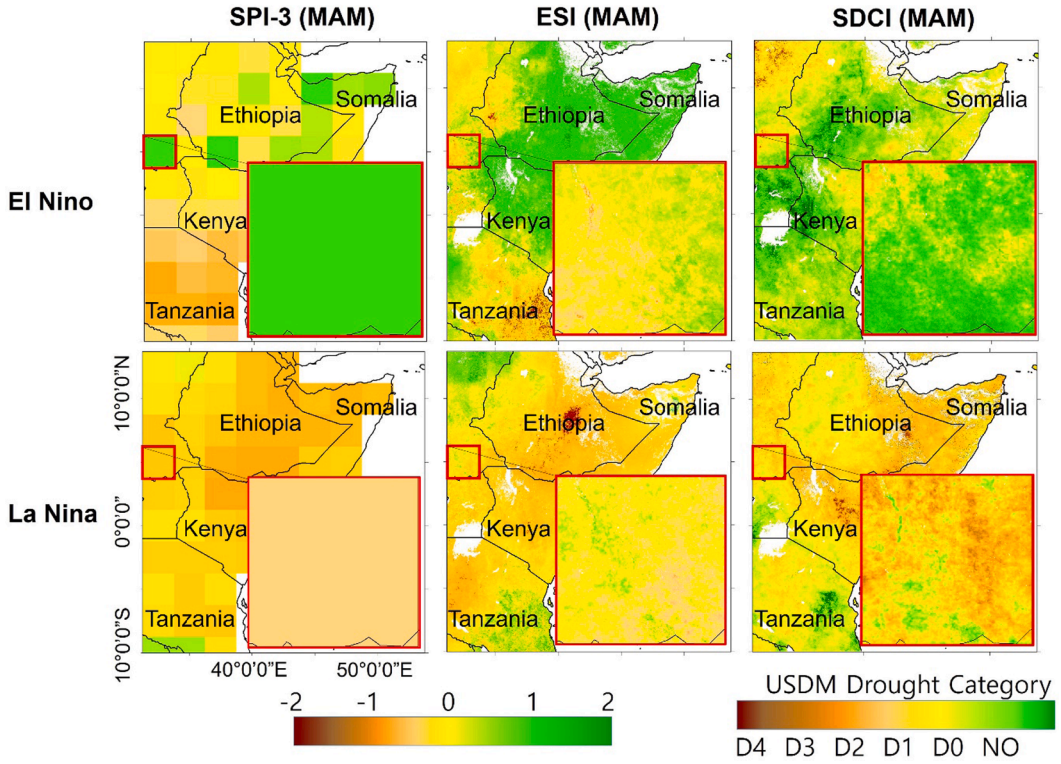

Fig. 7. Spatial distribution of the three drought indices—SPI-3, ESI, and SDCI—during MAM for El Niño and La Niña events.

high-resolution measurements, which provide greater details on the spatial domain when compared to the reanalysis data.

The strengthened ENSO relationship during MAM is possibly associated with the changes in the Walker circulation with a westward extension (Williams and Funk, 2011) and intensification (England et al., 2014), which is consistent with the enhanced ENSO teleconnection with stronger zonal SST gradients in the tropical Pacific (Hoell et al., 2013). It still remains controversial but the global climate models (GCMs) with a global warming scenario tend to predict weakening Walker circulation in the future, which is analogous to the pattern in El Niño (Vecchi et al., 2006), while faster warming is expected over the Maritime continent and eastern Pacific than that of the central Pacific (Cai et al., 2015). If the intensified relationship between ENSO and East African long rain for 2000–2016 is maintained in the future, it requires further research on dynamical mechanisms underlying decadal modulation of the ENSO teleconnection. The East African climate paradox, which is a term indicating a majority of increasing rainfall predictions by climate models with increasing carbon dioxide versus a recent dry

Fig. 8. Temporal patterns of the three drought indices—SPI (-1, -3, -6, -9, and -12), ESI, and SDCI—during MAM and OND. Drought indices were averaged within the red box shown in Fig. 7.

trend in East African long rain, could be explained by the recent La Niña-like trend with decreasing long rain and the El Niño-like trend with increasing long rain in the future scenarios. In this regard, further examinations are required to better understand ENSO-related modulations to the East African drought and seasonal outlook in the future.

Declaration of Competing Interest

The authors declare that they have no known competing financial interests or personal relationships that could have appeared to influence the work reported in this paper.

Acknowledgements

This research was supported by 'Satellite Data Applications' of the Korea Aerospace Research Institute (FR20G00), the National Research Foundation of Korea (NRF- 2017M1A3A3A02015981; NRF-2017R1D1A1B03028129; NRF-2018K2A9A2A06023758), and the Korea Meteorological Administration (KMIPA 2017-7010). CY was also supported by Global PhD Fellowship Program through the National Research Foundation of Korea (NRF), funded by the Ministry of Education (NRF-2018H1A2A1062207).

Appendix A. Supplementary material

Supplementary data to this article can be found online at https://doi.org/10.1016/j.isprsjprs.2020.02.003.

References

Adler, R.F., Huffman, G.J., Chang, A., Ferraro, R., Xie, P.-P., Janowiak, J., Rudolf, B., Schneider, U., Curtis, S., Bolvin, D., 2003. The version-2 global precipitation climatology project (GPCP) monthly precipitation analysis (1979–present). J. Hydrometeorol. 4, 1147–1167.

Anderson, M.C., Hain, C., Wardlow, B., Pimstein, A., Mecikalski, J.R., Kustas, W.P., 2011. Evaluation of drought indices based on thermal remote sensing of evapotranspiration over the continental United States. J. Clim. 24, 2025–2044.

Anderson, W., Zaitchik, B., Hain, C., Anderson, M., Yilmaz, M., Mecikalski, J., Schultz, L., 2012. Towards an integrated soil moisture drought monitor for East Africa. Hydrol. Earth Syst. Sci. 16, 2893–2913.

Asbury, Z., Aly, M., 2019. A geospatial study of the drought impact on surface water reservoirs: study cases from Texas, USA. GIScience Remote Sens. 56, 894–910.

Bayissa, Y.A., Tadesse, T., Svoboda, M., Wardlow, B., Poulsen, C., Swigart, J., Andel, S.J.V., 2019. Developing a satellite-based combined drought indicator to monitor agricultural drought: a case study for Ethiopia. GIScience Remote Sens. 56, 718–748. https://doi.org/10.1080/15481603.2018.1552508.

Barbosa, H., Kumar, T., Paredes, F., Elliott, S., Ayuga, J., 2019. Assessment of Caatinga response to drought using Meteosat-SEVIRI Normalized Difference Vegetation Index (NDVI) 2008–2016. ISPRS J. Photogramm. Remote Sens. 148, 235–252.

Bhuiyan, C., Saha, A.K., Bandyopadhyay, N., Kogan, F.N., 2017. Analyzing the impact of thermal stress on vegetation health and agricultural drought – a case study from Gujarat, India. GIScience Remote Sens. 54, 678–699.

Brands, S., 2017. Which ENSO teleconnections are robust to internal atmospheric variability? Geophys. Res. Lett. 44, 1483–1493.

Burrough, S., Thomas, D., 2013. Central southern Africa at the time of the African Humid Period: a new analysis of Holocene palaeoenvironmental and palaeoclimate data. Quat. Sci. Rev. 80, 29–46.

Cai, W., Santoso, A., Wang, G., Yeh, S.-W., An, S.-I., Cobb, K.M., Collins, M., Guilyardi, E., Jin, F.-F., Kug, J.-S., 2015. ENSO and greenhouse warming. Nat. Clim. Change 5, 849.

Cattani, E., Merino, A., Levizzani, V., 2016. Evaluation of monthly satellite-derived precipitation products over East Africa. J. Hydrometeorol. 17, 2555–2573.

d'Andrimont, R., Defourny, P., 2018. Monitoring African water bodies from twice-daily MODIS observation. GIScience Remote Sens. 55, 130–153.

Du, L., Tian, Q., Yu, T., Meng, Q., Jancso, T., Udvardy, P., Huang, Y., 2013. A comprehensive drought monitoring method integrating MODIS and TRMM data. Int. J. Appl. Earth Obs. Geoinf. 23, 245–253.

Edwards, D.C., 1997. Characteristics of 20th century drought in the United States at multiple time scales. In: AIR FORCE INST OF TECH WRIGHT-PATTERSON AFB OH.

England, M.H., McGregor, S., Spence, P., Meehl, G.A., Timmermann, A., Cai, W., Gupta, A.S., McPhaden, M.J., Purich, A., Santoso, A., 2014. Recent intensification of wind-driven circulation in the Pacific and the ongoing warming hiatus. Nat. Clim. Change 4, 222.

Goddard, L., Graham, N.E., 1999. Importance of the Indian Ocean for simulating rainfall anomalies over eastern and southern Africa. J. Geophys. Res.: Atmos. 104, 19099–19116.

Ghulam, A., Qin, Q., Teyip, T., Li, Z.-L., 2007a. Modified perpendicular drought index (MPDI): a real-time drought monitoring method. ISPRS J. Photogramm. Remote Sens. 62 (2), 150–164.

Ghulam, A., Qin, Q., Zhan, Z., 2007b. Designing of the perpendicular drought index. Environ. Geol. 52 (6), 1045–1052.

Hastenrath, S., 2000. Zonal circulations over the equatorial Indian Ocean. J. Clim. 13, 2746–2756.

Hastenrath, S., Polzin, D., Mutai, C., 2007. Diagnosing the 2005 drought in equatorial East Africa. J. Clim. 20, 4628–4637.

Hoell, A., Barlow, M., Saini, R., 2013. Intraseasonal and seasonal-to-interannual Indian Ocean convection and hemispheric teleconnections. J. Clim. 26, 8850–8867.

Hoell, A., Funk, C., 2014. Indo-Pacific sea surface temperature influences on failed consecutive rainy seasons over eastern Africa. Clim. Dyn. 43, 1645–1660.

Huffman, G.J., Adler, R.F., Arkin, P., Chang, A., Ferraro, R., Gruber, A., Janowiak, J., McNab, A., Rudolf, B., Schneider, U., 1997. The global precipitation climatology project (GPCP) combined precipitation dataset. Bull. Am. Meteorol. Soc. 78, 5–20.

Joly, M., Voldoire, A., 2009. Influence of ENSO on the West African monsoon: temporal aspects and atmospheric processes. J. Clim. 22, 3193–3210.

Kanamitsu, M., Ebisuzaki, W., Woollen, J., Yang, S., Hnilo, J., Fiorino, M., Potter, G., 2002. NCEP–DOE AMIP-II Reanalysis (R-2) Bulletin of the American Meteorological Society. 83, pp. 1631–1643. doi: 10.1175. In: BAMS-83-11-1631.[Cross Ref].

Keshavarz, M.R., Vazifedoust, M., Alizadeh, A., 2014. Drought monitoring using a Soil Wetness Deficit Index (SWDI) derived from MODIS satellite data. Agric. Water Manag. 132, 37–45.

Kogan, F., 1990. Remote sensing of weather impacts on vegetation in non-homogeneous areas. Int. J. Remote Sens. 11, 1405–1419.

Kogan, F.N., 1995. Application of vegetation index and brightness temperature for drought detection. Adv. Space Res. 15, 91–100.

Lee, C., Sohn, E., Park, J., Jang, J., 2019. Estimation of soil moisture using deep learning based on satellite data: a case study of South Korea. GIScience Remote Sens. 56, 43–67.

Levin, N.E., Zipser, E.J., Cerling, T.E., 2009. Isotopic composition of waters from Ethiopia and Kenya: insights into moisture sources for eastern Africa. J. Geophys. Res.: Atmos. 114.

Liebmann, B., Hoerling, M.P., Funk, C., Bladé, I., Dole, R.M., Allured, D., Quan, X., Pegion, P., Eischeid, J.K., 2014. Understanding recent Eastern Horn of Africa rainfall variability and change. J. Clim. 27, 8630–8645.

Lott, F.C., Christidis, N., Stott, P.A., 2013. Can the 2011 East African drought be attributed to human-induced climate change? Geophys. Res. Lett. 40, 1177–1181.

Lu, B., Ren, H.-L., Eade, R., Andrews, M., 2018. Indian Ocean SST modes and their impacts as simulated in BCC CSM1.1(m) and HadGEM3. Adv. Atmos. Sci. 35 (8), 1035–1048. https://doi.org/10.1007/s00376-018-7279-3.

Lyon, B., 2004. The strength of El Niño and the spatial extent of tropical drought. Geophys. Res. Lett. 31 (21).

Lyon, B., Barnston, A.G., 2005. ENSO and the spatial extent of interannual precipitation extremes in tropical land areas. J. Clim. 18 (23), 5095–5109.

Lyon, B., 2014. Seasonal drought in the Greater Horn of Africa and its recent increase during the March–May long rains. J. Clim. 27, 7953–7975.

Lyon, B., DeWitt, D.G., 2012. A recent and abrupt decline in the East African long rains. Geophys. Res. Lett. 39.

Maidment, R.I., Allan, R.P., Black, E., 2015. Recent observed and simulated changes in precipitation over Africa. Geophys. Res. Lett. 42, 8155–8164.

McKee, T., Doesken, N., Kleist, J., 1993. Proceedings of the 8th Conference on Applied Climatology, American Meteorology Society, 17–22 January, Anaheim, CA.

Nicholson, S.E., 1996. A review of climate dynamics and climate variability in Eastern Africa. Limnology, Climatology Paleoclimatology East African Lakes 25–56.

Nicholson, S.E., 2015. Long-term variability of the East African 'short rains' and its links to large-scale factors. Int. J. Climatol. 35, 3979–3990.

Nicholson, S.E., 2018. The ITCZ and the seasonal cycle over equatorial Africa. Bull. Am. Meteorol. Soc. 99, 337–348.

Nicholson, S.E., Kim, J., 1997. The relationship of the El Niño-Southern oscillation to African rainfall. Int. J. Climatol. 17, 117–135.

Otkin, J.A., Anderson, M.C., Hain, C., Mladenova, I.E., Basara, J.B., Svoboda, M., 2013. Examining rapid onset drought development using the thermal infrared–based evaporative stress index. J. Hydrometeorol. 14, 1057–1074.

Otkin, J.A., Anderson, M.C., Hain, C., Svoboda, M., Johnson, D., Mueller, R., Tadesse, T., Wardlow, B., Brown, J., 2016. Assessing the evolution of soil moisture and vegetation conditions during the 2012 United States flash drought. Agric. For. Meteorol. 218, 230–242.

Padhee, S.K., Nikam, B.R., Dutta, S., Aggarwal, S.P., 2017. Using satellite-based soil moisture to detect and monitor spatiotemporal traces of agricultural drought over Bundelkhand region of India. Giscience Remote Sens. 54, 144–166.

Park, S., Im, J., Jang, E., Rhee, J., 2016. Drought assessment and monitoring through blending of multi-sensor indices using machine learning approaches for different climate regions. Agric. For. Meteorol. 216, 157–169.

Park, S., Im, J., Park, S., Rhee, J., 2017. Drought monitoring using high resolution soil moisture through multi-sensor satellite data fusion over the Korean peninsula. Agric. For. Meteorol. 237, 257–269.

Peng, J., Dadson, S., Hirpa, F., Dyer, E., Lees, T., Miralles, D., Funk, C., 2019. A pan-African high resolution drought index dataset. Earth Syst. Sci. Data. https://doi.org/10.5194/essd-2019-138.

Rayner, N., Parker, D.E., Horton, E., Folland, C., Alexander, L., Rowell, D., Kent, E., Kaplan, A., 2003. Global analyses of sea surface temperature, sea ice, and night marine air temperature since the late nineteenth century. J. Geophys. Res.: Atmos 108.

Rhee, J., Im, J., Carbone, G.J., 2010. Monitoring agricultural drought for arid and humid regions using multi-sensor remote sensing data. Remote Sens. Environ. 114,

2875–2887.
Ryu, J.H., Han, K.S., Lee, Y.W., Park, N.W., Hong, S., Chung, C.Y., Cho, J., 2019. Different agricultural responses to extreme drought events in neighboring counties of South and North Korea. Remote Sens. 11 (15), 1773.
Saji, N., Goswami, B., Vinayachandran, P., Yamagata, T., 1999. A dipole mode in the tropical Indian Ocean. Nature 401, 360.
Schneider, U., Fuchs, T., Meyer-Christoffer, A., Rudolf, B., 2008. Global precipitation analysis products of the GPCC. Global Precipitation Climatology Centre (GPCC), DWD, Internet Publikation, 112.
Schreck III, C.J., Semazzi, F.H., 2004. Variability of the recent climate of eastern Africa. Int. J. Climatology: A J. Royal Meteorological Soc. 24, 681–701.
Senay, G.B., Verdin, J., 2003. Characterization of yield reduction in Ethiopia using a GIS-based crop water balance model. Can. J. Remote Sens. 29, 687–692.
Sheffield, J., Wood, E.F., Chaney, N., Guan, K., Sadri, S., Yuan, X., Olang, L., Amani, A., Ali, A., Demuth, S., 2014. A drought monitoring and forecasting system for sub-Sahara African water resources and food security. Bull. Am. Meteorol. Soc. 95, 861–882.
Tadesse, T., Champagne, C., Wardlow, B., Hadwen, T., Brown, J., Demisse, G., Bayissa, Y., Davidson, A., 2017. Building the vegetation drought response index for Canada (VegDRI-Canada) to monitor agricultural drought: first results. GIScience Remote Sens. 54, 230–257.
Tierney, J.E., Smerdon, J.E., Anchukaitis, K.J., Seager, R., 2013. Multidecadal variability in East African hydroclimate controlled by the Indian Ocean. Nature 493, 389.
Timmermann, A., An, S.-I., Kug, J.-S., Jin, F.-F., Cai, W., Capotondi, A., Cobb, K., Lengaigne, M., McPhaden, M.J., Stuecker, M.F., 2018. El Niño-Southern Oscillation complexity. Nature 559, 535.
Tran, H.T., Campbell, J.B., Tran, T.D., Tran, H.T., 2017. Monitoring drought vulnerability using multispectral indices observed from sequential remote sensing (Case Study: Tuy Phong, Binh Thuan, Vietnam). Giscience Remote Sens. 54, 167–184.
Vecchi, G.A., Soden, B.J., Wittenberg, A.T., Held, I.M., Leetmaa, A., Harrison, M.J., 2006. Weakening of tropical Pacific atmospheric circulation due to anthropogenic forcing. Nature 441, 73.
Viste, E., Sorteberg, A., 2013. Moisture transport into the Ethiopian highlands. Int. J. Climatol. 33, 249–263.
Wang, J., Ling, Z., Wang, Y., Zeng, H., 2016. Improving spatial representation of soil moisture by integration of microwave observations and the temperature-vegetation-drought index derived from MODIS products. ISPRS J. Photogramm. Remote Sens. 113, 144–154.
Williams, A.P., Funk, C., 2011. A westward extension of the warm pool leads to a westward extension of the Walker circulation, drying eastern Africa. Clim. Dyn. 37, 2417–2435.
Zhang, A., Jia, G., 2013. Monitoring meteorological drought in semiarid regions using multi-sensor microwave remote sensing data. Remote Sens. Environ. 134, 12–23.
Zhang, L., Jiao, W., Zhang, H., Huang, C., Tong, Q., 2017. Studying drought phenomena in the Continental United States in 2011 and 2012 using various drought indices. Remote Sens. Environ. 190, 96–106.
Zheng, X.-T., Xie, S.-P., Liu, Q., 2011. Response of the Indian Ocean basin mode and its capacitor effect to global warming. J. Clim. 24, 6146–6164.